

Article

VSG-Based Dynamic Frequency Support Control for Autonomous PV–Diesel Microgrids

Rongliang Shi  and Xing Zhang *

School of Electrical Engineering and Automation, Hefei University of Technology, Hefei 230009, China; shirl163@163.com

* Correspondence: honglf@ustc.edu.cn; Tel.: +86-551-6290-1408; Fax: +86-551-6290-1408

Received: 3 June 2018; Accepted: 5 July 2018; Published: 11 July 2018



Abstract: This paper demonstrates the use of a novel virtual synchronous generator (VSG) to provide dynamic frequency support in an autonomous photovoltaic (PV)–diesel hybrid microgrid with an energy storage system (ESS). Due to the lack of enough rotating machines, PV fluctuation might give rise to unacceptable frequency excursions in the microgrid. The VSG entails controlling the voltage-source inverter (VSI) to emulate a virtual inertia and a virtual damping via power injection from/to the ESS. The effect of the VSG on the frequency is investigated. The virtual inertia decreases the maximum frequency deviation (MFD) and the rate of change of frequency (RoCoF), but in exchange for raising the virtual inertia, the system is more oscillating. Meanwhile, raising the virtual damping brings reductions in the amplitude of the oscillations of frequency. However, the dynamic frequency support provided by them is lagging behind. In this regard, an improved VSG based on the differential feedforward of the diesel generator set (DGS) output current is proposed to further mitigate the MFD and the RoCoF. Simulations and experimental results from an autonomous microgrid consisted of a 400 kW DGS, and a 100 kVA VSG are provided to validate the discussion.

Keywords: virtual synchronous generator; dynamic frequency support; autonomous microgrid; virtual inertia; virtual damping; differential feedforward

1. Introduction

Photovoltaic (PV)–diesel hybrid microgrids are a fine choice for electricity generation in isolated regions where PV resource is rich [1]. The microgrid is constructed by a reduced number of controlled diesel generator sets (DGSs), and solar resources are used to supplement power generation [2]. However, the frequency excursions are more likely to happen in autonomous microgrids than in large interconnected power grids, since they feature rapid changes in the power demands and a relatively small generation capacity, especially in a high penetration power system with many intermittent renewable generators [3]. Furthermore, if DGS units cannot keep the maximum frequency deviation (MFD) as well as the rate of change of frequency (RoCoF) within stipulated operating ranges, skipping of power generators and loads may occur [4]. Hence, the help of energy storage systems (ESSs) is required to keep the dynamic stability of frequency for the self-existent microgrid.

Different solutions can be found in the control strategies of a voltage-source inverter (VSI) with an ESS. An ESS-based dynamic frequency support solution is used to cope with system frequency deviation by filtering of the output power of stochastic resources [5]. Nevertheless, this strategy needs the measurement of the output power, which requires a communication bus. The droop method is used to control the distributed energy storage interfaces independently by the local measurements, without a communication bus [6–10]. However, this strategy is aimed to provide only frequency adjustment by employing the permanent frequency droop form, thus, it cannot deal with the problem of dynamic frequency regulation. In virtual synchronous generator (VSG) method, which is VSI based, the ESS

is managed in a way to emulate a virtual inertia and a virtual damping of a synchronous generator (SG) [11–18].

The constant parameters (CP)-VSG used to provide dynamic frequency support involves exhibiting the damping power and the inertial response of a real conventional SG [19,20]. The emulation of inertial response generally involves the domination of power that is inversely proportional to the first time derivative of the frequency [21]. On the other hand, the virtual damping control helps to weaken fluctuations, and then, decrease the settling time of the frequency [22]. Nevertheless, they do not investigate the use of the adjustable virtual parameters that can adjust their values during operation. As a result, the self-tuning (ST)-VSG with the variable virtual parameters is operating as a controlled current source, which is used to attenuate the frequency fluctuations [4]. However, the online optimization is asked to maintain the virtual damping power and the inertial response, which raises the calculation amount of the digital signal processor (DSP). Whereas, for the microgrid applications, especially considering the islanding mode, the VSG is selected to run with a voltage control method (VCM), as it is able to provide enough frequency and voltage support for the loads [23]. In this regard, the bang–bang control strategy with the variable virtual inertia is proposed to attenuate the frequency fluctuations [24]. The sign of the derivative of angular velocity with respect to the sign of the relative angular velocity defines the acceleration or deceleration. They act in the same direction, therefore, it is an acceleration period. In addition, as they have opposite signs, it is a deceleration. By choosing a large value for the moment of inertia during acceleration, the haste is decreased. During deceleration, a small value for inertia factor is used to improve the deceleration effect. In other words, the virtual inertia is changed between a large value of inertia and a small one for four times during each cycle of fluctuations. Unfortunately, using a large constant virtual inertia for the bang–bang control will lead to a sluggish response. In addition, each switching may cause the power fluctuations.

Despite the effectiveness of the above techniques, the inertial response, as well as the damping power of the CP-VSG or the ST-VSG, are realized by measuring both the frequency variations and the frequency deviations from the nominal grid frequency value. As a result, the dynamic frequency support provided by the inertial response as well as the damping power is behind the variations of loads. Thus, the effect of improving the frequency stability using the inertial response and the damping power is limited. In this regard, an improved VSG based on the differential feedforward of the DGS output current is proposed to further mitigate the MFD and the RoCoF.

This paper is organized as follows. In Section 2, the structure of an autonomous microgrid and the control model of a DGS are reviewed. Section 3 analyzes the impacts of the inertial response as well as the damping power of the VSG on the frequency stability. Section 4 explains the proposed VSG with the differential feedforward of the DGS output current and its performance evaluation. In Section 5, simulations and experimental results from an autonomous microgrid consisting of a 400 kW DGS and a 100 kVA VSG are demonstrated. Section 6 is devoted to the conclusion.

2. System Overview

Figure 1 shows a typical system structure of an autonomous PV–battery–diesel microgrid based on a PV generator, two VSI units, and a DGS working in parallel. For each space vector pulse width modulation (SVPWM) VSI unit, the dc power is supplied by an ESS, and a fixed dc voltage is assumed in this paper to simplify the theoretic analysis. Each VSI unit is integrated to the ac-bus through a LC filter and a distribution transformer (DT). The VSI can inject power either into the ac-bus—inverter mode, or into the ESS—rectifier mode. Depending on the proportion between PV and ESS power, the microgrid operation can be characterized as a low PV penetration level and a high PV penetration level.

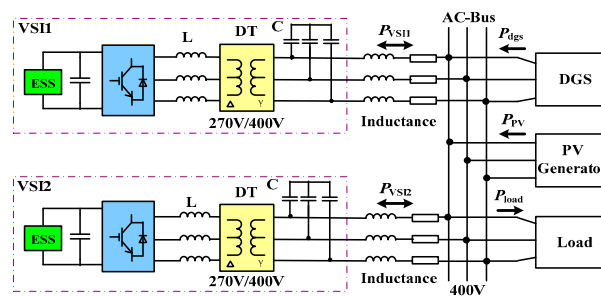


Figure 1. Typical structure of an autonomous photovoltaic (PV)-battery-diesel microgrid.

Based on a DGS unit and two VSI units running in parallel, the power contribution of the PV generator is relatively small, i.e., the autonomous microgrid operates with a low PV penetration. In this situation, frequency variations due to PV fluctuations would be in an appropriate limit. The active power balance in the ac-bus is given by

$$P_{VSI1} + P_{VSI2} + P_{dgs} + P_{PV} = P_{load}, \tag{1}$$

where P_{VSI1} , P_{VSI2} , P_{dgs} , P_{PV} , and P_{load} are the VSI units, DGS, PV generator, and load instantaneous active powers, respectively.

On the other hand, for a certain load condition, only one VSI and a DGS operating in isochronous mode will be service. Under this circumstance, the power dedication of the solar source might be comparatively high, i.e., the microgrid would run in high PV penetration. As a result, PV fluctuations would produce unacceptable frequency variations. However, the frequency variations result in rapid acceleration or deceleration of the DGS rotor, and they can be mitigated with a suitable control method. The active power balance in the ac-bus is given by

$$P_{VSI} + P_{dgs} + P_{PV} = P_{load}, \tag{2}$$

where P_{VSI} is the active power of the VSI in service.

As illustrated before, this paper concentrates on the situation when the autonomous microgrid is exposed to a high PV penetration. For purpose of analysis, it is assumed that the voltage amplitude of the ac-bus is regulated, and it is considered constant.

The DGS model is made up of two major components coupled by a collaborative shaft: the diesel prime mover and the SG. Due to the scope of this paper, the speed control schematic diagram of the DGS with a proportional-integrative (PI) controller is shown in Figure 2, according to [1].

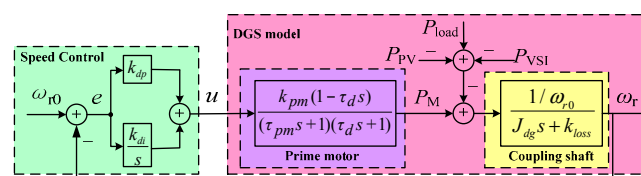


Figure 2. Diesel generator set (DGS) speed control based on a proportional-integrative (PI) controller.

In Figure 2, J_{dg} is the rotating inertia, ω_r is the rotor angular speed, and k_{loss} represents the rotational losses, ω_{r0} is the synchronous speed, P_M is the mechanical power supplied by the prime motor, k_{pm} concentrates the gain of fuel injection system and diesel engine, τ_{pm} is the time constant of the fuel injection system, τ_d is the dead time of the diesel engine, k_{dp} and k_{di} are the proportional and integral factors of a PI controller. The parameters of a 26 kW DGS obtained from [25] are shown in Table 1.

Table 1. The main parameters of the diesel generator set (DGS).

Parameter	Value	Parameter	Value
k_{pm}	1	τ_d	0.011 s
ω_{r0}	314.16 rad/s	k_{loss}	0.02 kg·m ² /s
J_{dg}	0.66 kg·m ²	τ_{pm}	0.2 s
k_{dp}	409.5	k_{di}	367.3

3. Impact of Virtual Synchronous Generator (VSG) on Frequency Stability

This section presents the utilization of a VSG to provide dynamic frequency control in an autonomous microgrid. Particularly, the VSG is realized with a VSI, and the method used to provide dynamic frequency support consists of simulating the damping power and the inertial response of a real SG, which are available only during a transient.

If the active power of the VSG is managed in inverse proportion to the derivative of the rotor speed, then promoting the inertial response of the DGS to variations in the power demand [4]. Hence, the active power of the VSG is defined as

$$P_{VSI} = -J\omega_{r0} \frac{d\omega_r}{dt}, \tag{3}$$

where J is the virtual inertia. The inertial response of the VSG simulates the power that is inherently absorbed or released by a real SG as the power demand changes [21]. When the rotor speed begins to reduce (a negative derivative), the VSG begins to inject active power into the system until the rotor speed attains its minimum (when the first derivative is zero), then the rotor speed begins to rise (a positive derivative), and then the VSG begins to absorb active power. This procedure will last until the new steady state is realized. Figure 3 shows the block diagram for speed control with the virtual inertia control loop.

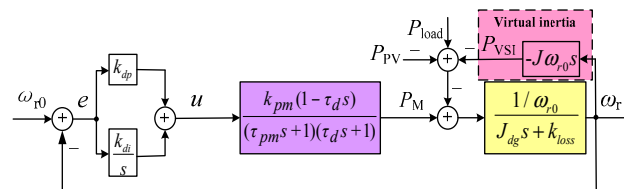


Figure 3. DGS speed control with the virtual inertia control loop.

From Figure 3, the transfer function in terms of the active powers as inputs can be obtained as follows:

$$G_J(s) = \frac{\omega_r(s)}{P_{PV}(s) - P_{load}(s)} = \frac{s}{(J_{eq}\omega_{r0} - k_{dp}\tau_d)s^2 + Ms + k_{di}}, \tag{4}$$

where $J_{eq} = (J_{dg} + J)$ is the total inertia, $M = (k_{loss}\omega_{r0} + k_{dp} - k_{di}\tau_d)$. On the basis of (4), the standard parameters of a second-order transient response with the virtual inertia loop can be defined as

$$\zeta_1 = \frac{M}{2\sqrt{k_{di}(J_{eq}\omega_{r0} - \tau_d k_{dp})}}, \quad \omega_{n1} = \frac{k_{di}}{\sqrt{k_{di}(J_{eq}\omega_{r0} - \tau_d k_{dp})}}, \tag{5}$$

where ω_{n1} is the natural oscillation frequency, ζ_1 is the damping ratio. From the (5), it could be established that, in exchange for adding the virtual inertia, the control system becomes more oscillatory and slower as the values of ζ_1 and ω_{n1} become smaller. Due to space limitations, the design of the virtual inertia is not discussed here, and more details are available in [26].

On the other hand, if the active power of the VSG is managed in proportion to the deviation of the rotor speed, then enhancing the damping power of the DGS leads to variations in the power demand. The active power of the VSG is defined as

$$P_{VSI} = D\omega_0(\omega_{r0} - \omega_r), \tag{6}$$

where D is the virtual damping of the VSG. The damping power is supplied by the virtual damper windings that help to weaken oscillations, and hence, reduce the stabilization time for a predefined tolerance band. Any deviation from the synchronous speed generates a power that tries to bring back the rotor speed to the reference [22]. Figure 4 shows the block diagram for speed control with the virtual damping control loop.

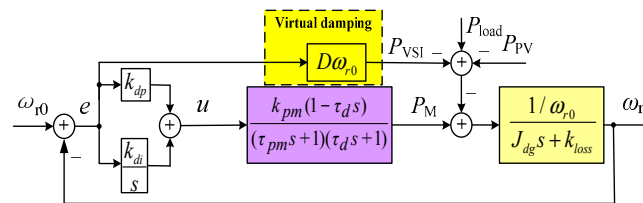


Figure 4. DGS speed control with the virtual damping control loop.

From Figure 4, the transfer function in terms of the active powers as inputs can be obtained as follows:

$$G_D(s) = \frac{\omega_r(s)}{P_{PV}(s) - P_{load}(s)} = \frac{s}{(J_{dg}\omega_{r0} - k_{dp}\tau_d)s^2 + Ns + k_{di}}, \tag{7}$$

where $N = [(k_{loss} + D)\omega_{r0} + k_{dp} - k_{di}\tau_d]$. On the basis of (7), the standard parameters of a second-order transient response with the virtual damping loop can be defined as

$$\zeta_2 = \frac{N}{2\sqrt{k_{di}(J_{dg}\omega_{r0} - \tau_d k_{dp})}}, \quad \omega_{n2} = \frac{k_{di}}{\sqrt{k_{di}(J_{dg}\omega_{r0} - \tau_d k_{dp})}}, \tag{8}$$

where ω_{n2} is the natural oscillation frequency, ζ_2 is the damping ratio. From (8), it could be concluded that more virtual damping would assist to stabilize the control system faster as the value of ζ_2 becomes bigger.

In order to evaluate the above analysis results, the control block diagrams of the simulation of an autonomous microgrid compensated with the VSG were built according to Figures 3 and 4. The tests consist of a step increase in the power output of the PV generator, P_{PV} , at $t = 8$ s from 0 kW to 10 kW, while the load power demand, P_{load} , remains constant at 15 kW. It should be noted that the PV production is connected to the microgrid by a PV inverter which is operating as a controlled current source. Then, a step increase in the power output of the PV generator can be achieved by regulating the PV inverter in this paper. In these conditions, the microgrid will operate at a high PV penetration level of 40%. The DGS parameters used in simulations are presented in Table 1. The suitable values of J and D can be determined by the (5) and (8) using the parameters listed in Table 1. Simulations are made for speed control without virtual inertia, $J = 0$, and with virtual inertia control, $J = 0.32$ kg·m² and $J = 0.64$ kg·m².

From Figure 5a, it can be seen that the key effect of increasing virtual inertia is that the MFD decreases. However, a side effect of increasing virtual inertia is that the frequency will oscillate for a longer time. Meanwhile, increasing the virtual damping obtains a reduction in the MFD, as can be seen from Figure 5b.

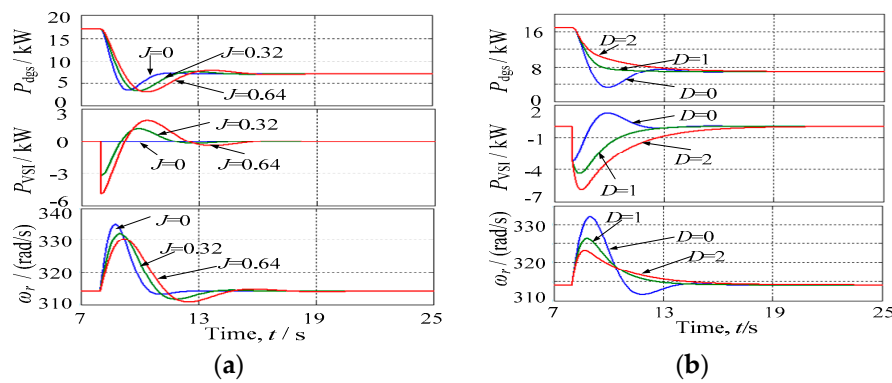


Figure 5. Effects of the inertia and damping on an active power transient. (a) Different values of virtual inertia and $D = 0$; (b) Different values of virtual damping and $J = 0.32 \text{ kg}\cdot\text{m}^2$.

As mentioned before, the virtual inertia as well as the virtual damping are performed by means of the ESS. Figure 5 also shows that the values of J and D are directly related to the expected dynamic performance and proper capacity of the ESS.

The angular frequency-acceleration trajectories of simulated DGS are shown in Figure 6. The advantage of adding the virtual inertia is the reduction of the RoCoF due to a power disturbance. For $J = 0.64 \text{ kg}\cdot\text{m}^2$, the maximum RoCoF is reduced from 8 Hz/s to 4 Hz/s, as can be seen from Figure 6a. From Figure 6b, it can be seen that the advantages of increasing the virtual damping are the attenuation of the amplitude of the oscillations of the frequency and the reduction of the MFD. For $D = 2$, the MFD is reduced from 2.85 Hz to 1.4 Hz.

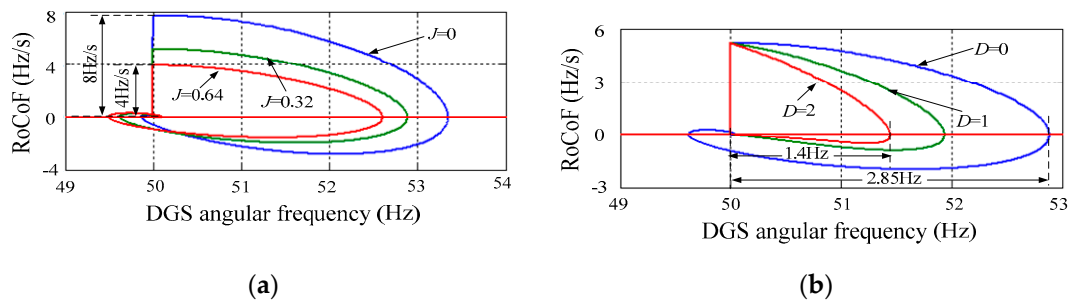


Figure 6. Angular frequency-acceleration curves of DGS with (a) virtual inertia control loop; (b) virtual damping control loop.

It is important to point out that, the variations of loads mainly result in the oscillations of the frequency. As a result, the changes of the latter lag behind the changes of the former. Since the inertial response as well as the damping power of the VSG are realized by measuring the variations of the frequency, thus, the dynamic frequency support provided by them is also lagging behind. In this regard, alternative approaches to provide a dynamic power response that can be synchronized with the variations of loads or even be ahead of the variations of loads.

4. Proposed VSG and Its Performance Evaluation

Considering that the first frequency oscillation is the most serious one in terms of maintaining the system frequency stability, an improved VSG based on the differential feedforward of the DGS output current is proposed to further decrease the MFD and the RoCoF. Note that the DGS output power can be approximately equal to its mechanical power under the condition of neglecting the mechanical

loss and the iron loss. As a result, the differential of the DGS output current can be replaced by the differential of its mechanical power, assuming that the voltage amplitude on the ac-bus is fixed.

In this case, the active power of the VSG based on the differential feedforward of the DGS output current is defined as

$$P_{VSI} = \frac{k_{df}s}{\tau s + 1} P_{dgs} \approx \frac{k_{df}s}{\tau s + 1} P_M, \tag{9}$$

where k_{df} is the differential feedforward gain, and τ is the filtering time gain of the low-pass filter (LPF). The active power is typically calculated from the time derivative of the DGS mechanical power that can expand the noise that is usually contained in this power. Hence, a LPF is applied to prevent the excessive noise from polluting the system. Figure 7 is the block diagram for speed control with the differential feedforward of the DGS output current control loop.

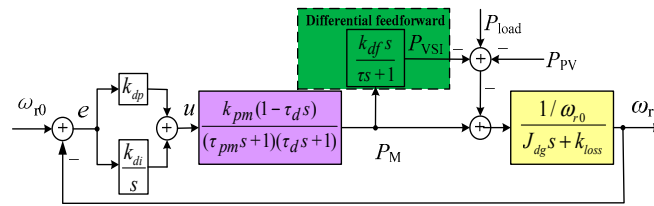


Figure 7. DGS speed control with the differential feedforward of its output current control loop.

From Figure 7, the transfer function in terms of the active powers as inputs can be obtained as follows:

$$G_{DF}(s) = \frac{\omega_r(s)}{P_{PV}(s) - P_{load}(s)} = \frac{(\tau s + 1)s}{as^3 + bs^2 + cs + k_{di}}, \tag{10}$$

where

$$\begin{cases} a = J_{dg}\omega_{r0}\tau - (\tau + k_{df})k_{dp}\tau_d \\ b = (k_{loss}\tau + J_{dg})\omega_{r0} - k_{dp}\tau_d + (k_{dp} - k_{di}\tau_d)(\tau + k_{df}) \\ c = k_{loss}\omega_{r0} + k_{dp} - k_{di}\tau_d + (\tau + k_{df})k_{di} \end{cases} . \tag{11}$$

Using (10) and (11), the trajectory of the three eigenvalues ($\lambda_1, \lambda_2, \lambda_3$) can be obtained. Figure 8a shows the trajectory of these eigenvalues as a function of the differential feedforward gain k_{df} . It can be seen that as k_{df} is increased, conjugate eigenvalues λ_1 and λ_2 move towards the real axis, making the system less oscillatory. Eigenvalue λ_3 moves towards the stable region, which makes the system evolve from a third-order system to an approximate second-order system. Meanwhile, Figure 8b shows the trajectory of these eigenvalues as a function of the filter time gain τ . It can be seen that as τ is increased, conjugate eigenvalues λ_1 and λ_2 move towards the real axis, making the system less oscillatory. Eigenvalue λ_3 moves towards the unstable region, which makes the system evolve from a second-order system to an approximate third-order system. Figure 8a,b have been obtained with the DGS parameters given in Table 1.

It is to be noted that a LPF with high cut-off frequency is required to enhance the dynamic response of the VSG, whereas a large filter time gain is required to obtain good attenuation of high frequency distortion components in the calculated active power and to increase the system damping. For this reason, and to operate without the distortion components, it is necessary to use larger τ values, like $\tau = 0.3$ s, or $\tau = 0.5$ s, but in exchange for longer dynamic reactions.

Based on the above analysis, simulations are made for speed control without differential feedforward, $k_{df} = 0$, and with differential feedforward control, $k_{df} = 1$ and $k_{df} = 2$. From Figure 9a, it can be seen that adding the differential feedforward gain produces a reduction in the MFD. Adding differential feedforward gain mitigates the MFD and the RoCoF effectively, due to a power disturbance. For $k_{df} = 2$, the MFD is reduced from 2.85 Hz to 0.85 Hz, and the RoCoF is decreased quickly, as can be seen from Figure 9b.

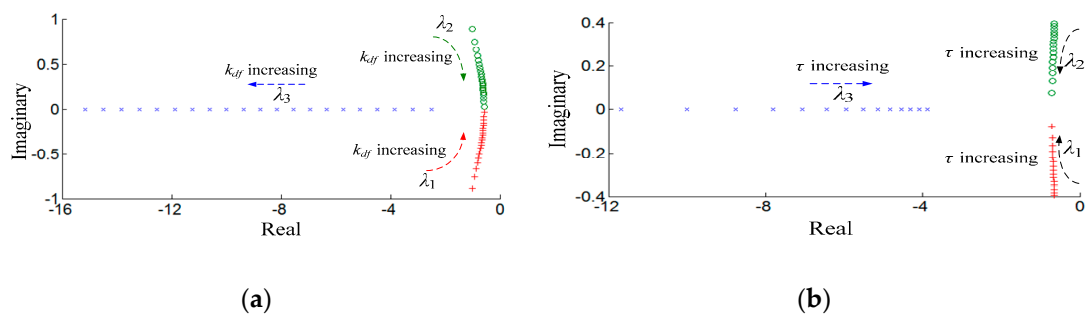


Figure 8. Traces of the three eigenvalues as a function of (a) differential feedforward gain: $\tau = 0.3$, $0 \leq k_{df} \leq 2$; (b) filter time gain: $k_{df} = 1$, $0.1 \leq \tau \leq 0.96$.

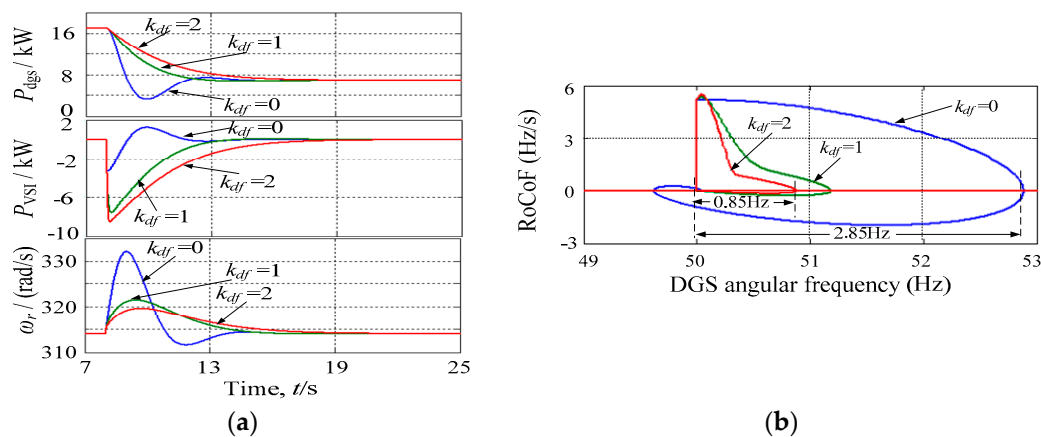


Figure 9. (a) Effects of the different differential feedforward gains ($D = 0$. and $J = 0.32 \text{ kg}\cdot\text{m}^2$) on an active power transient; (b) Angular frequency-acceleration curves of DGS with differential feedforward control loop.

The proposed control method for the DGS is implemented as shown in Figure 10. This control scheme can provide virtual inertia, virtual damping, and differential feedforward control for the DGS to support dynamic frequency control.

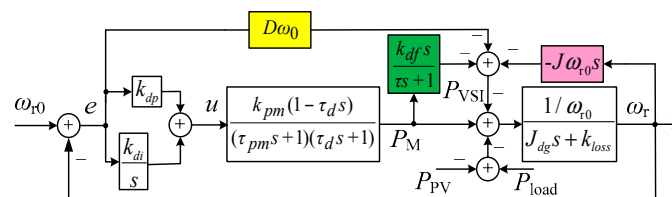


Figure 10. Proposed control strategy for the DGS to support dynamic frequency control.

With Figure 10, the angular frequency-acceleration trajectories of simulated DGS are shown in Figure 11. It is obvious that the MFD and the RoCoF are mitigated more effectively for $J = 0.32 \text{ kg}\cdot\text{m}^2$, $D = 1$, $k_{df} = 2$ than for $J = 0.32 \text{ kg}\cdot\text{m}^2$, $D = 1$, $k_{df} = 1$, or for $J = 0.32 \text{ kg}\cdot\text{m}^2$, $D = 1$, $k_{df} = 0$, or for $J = 0.32 \text{ kg}\cdot\text{m}^2$, $D = 0$, $k_{df} = 0$. It implies that the proposed VSG with the differential feedforward control loop is more effective in enhancing the system frequency stability than the VSG without the differential feedforward control loop.

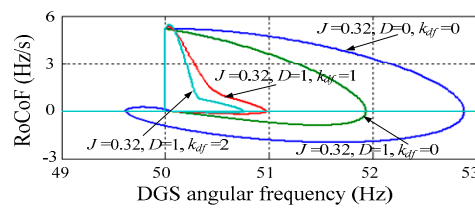


Figure 11. Angular frequency-acceleration curves of DGS with virtual inertia, virtual damping, or differential feedforward control loop.

5. Simulation and Experimental Results

The proposed VSG control strategy for the DGS to support dynamic frequency control is confirmed through Matlab/Simulink (R2011b, MathWorks, Natick, MA, USA), and experimentally on an autonomous microgrid. Figure 12 describes the schematic of the simulation and experiment of the microgrid consisted of a 100 kVA VSG and a 400 kW DGS for a load step of 100 kW at $t = 3$ s. The system parameters of the simulation, as well as the experiments, are almost the same, and are enumerated in Table 2.

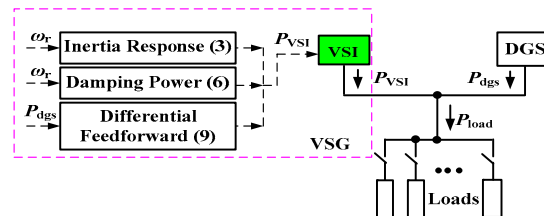


Figure 12. An autonomous microgrid with a DGS and a virtual synchronous generator (VSG) unit.

Table 2. Parameters in the simulation and experiment.

The 100 kVA VSG System		
Parameter	Simulation	Experiment
System voltage	380 V, 50 Hz	380 V, 50 Hz
DC link voltage	600 V	600 V
LC filter	$L = 0.56$ mH, $C = 270$ μ F	$L = 0.56$ mH, $C = 270$ μ F
Power reference	$P_{ref} = 20$ kW, $Q_{ref} = 0$	$P_{ref} = 20$ kW, $Q_{ref} = 0$
Switching frequency	5 kHz	5 kHz
The 400 kW DGS System		
Parameter	Simulation	Experiment
System voltage	380 V, 50 Hz	380 V, 50 Hz
Total inertia	3.6 kg·m ²	3.6 kg·m ²
Rotational loss	0.24 kg·m ² /s	0.24 kg·m ² /s
Fuel injection time	60 ms	60 ms
Engine delay	15 ms	15 ms
Governor gains	$K_p = 0.16$, $K_i = 0.9$	$K_p = 0.16$, $K_i = 0.9$
AVR gains	$k_p = 0.12$, $k_i = 0.12$	$k_p = 0.12$, $k_i = 0.12$

A. Simulation verification

(1) Virtual inertia: From Figure 13a, it can be seen that a side effect of increasing virtual inertia is that the system frequency will oscillate for a longer time. However, increasing virtual inertia reduces the MFD and the RoCoF effectively due to a power disturbance. For $J = 6$ kg·m², the MFD is decreased from 0.5 Hz to 0.45 Hz and the maximum RoCoF is decreased from 3.2 Hz/s to 2 Hz/s, as can be seen from Figure 13b.

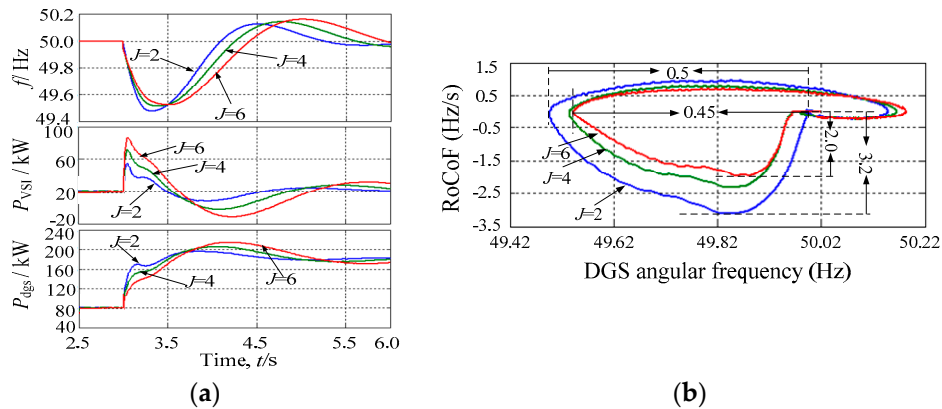


Figure 13. (a) Effects of the different values of virtual inertia and zero virtual damping on an active power transient; (b) Angular frequency-acceleration curves of DGS with virtual inertia control loop.

(2) Virtual damping: The same tests are conducted for the VSG with the added virtual damping to support dynamic frequency control on an active power transient. Figure 14a displays the simulation results for the alterations of the system frequency, the output active powers of the VSG, and the DGS. It is observed that the advantages of adding virtual damping to the system are the attenuation of the amplitude of the oscillations of the frequency and the reduction of the MFD.

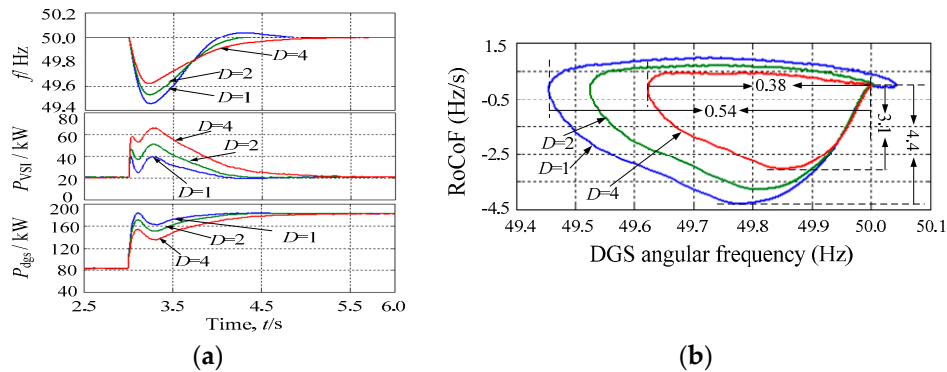


Figure 14. (a) Effects of the different values of virtual damping and zero virtual inertia on an active power transient; (b) Angular frequency-acceleration curves of DGS with virtual damping control loop.

From Figure 14b, it can be seen that the curve “ $D = 4$ ” illustrates the RoCoF and the MFD with respect to the rated value that situates inside the other two curves. It explains that increasing the virtual damping produces reductions in the MFD and the RoCoF. For $D = 4$, the MFD is reduced from 0.54 Hz to 0.38 Hz, and the maximum RoCoF is reduced from 4.4 Hz/s to 3.1 Hz/s.

(3) Differential feedforward: Figure 15a displays the simulation results for the alterations of the system frequency, the output active powers of the VSG, and the DGS. It is observed that the advantages of adding the differential feedforward gain are the attenuation of the amplitude of the oscillations of the frequency and the reduction of the MFD. On the other hand, the curve “ $k_{df} = 4$ ” illustrates the RoCoF and the MFD with respect to the rated value that situates inside the other two curves. It explains that increasing the differential feedforward gain mitigates both the MFD and the RoCoF effectively. For $k_{df} = 4$, the MFD is reduced from 0.45 Hz to 0.29 Hz, and the maximum RoCoF is reduced from 2.3 Hz/s to 1.1 Hz/s, as can be seen from Figure 15b.

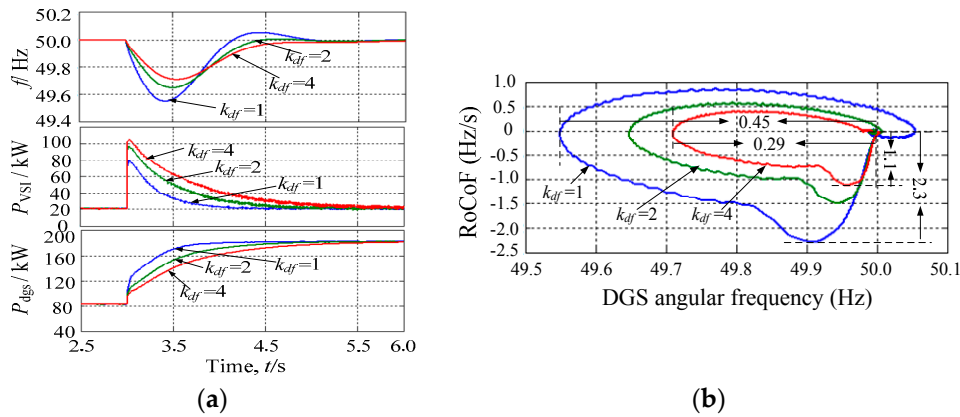


Figure 15. (a) Effects of the different differential feedforward gains ($D = 0$ and $J = 0$) on an active power transient; (b) Angular frequency-acceleration curves of DGS with differential feedforward control loop.

B. Experimental verification

Experiments are also carried out on an autonomous microgrid consisting of a 100 kVA VSG and a 400 kW DGS for a load step of 100 kW to verify the proposed VSG-based dynamic frequency support scheme. In the experiments, a three-phase programmable rectifier is used to represent the ESS, and the three-phase VSG system is controlled by a TMS320F28335 DSP (TMS320C28x, Texas Instruments, Dallas, TX, USA), which implements the proposed control strategies, as described in the previous sections. The VSG unit consists of a three-phase IGBT full bridge with a switching frequency of 5 kHz and an LC output filter, using the parameters listed in Table 2. The experimental platform of the autonomous microgrid is shown in Figure 16. The transitory regime is created by switching a resistive load of 100 kW on at certain time intervals in the experiment as shown in Figure 16a.

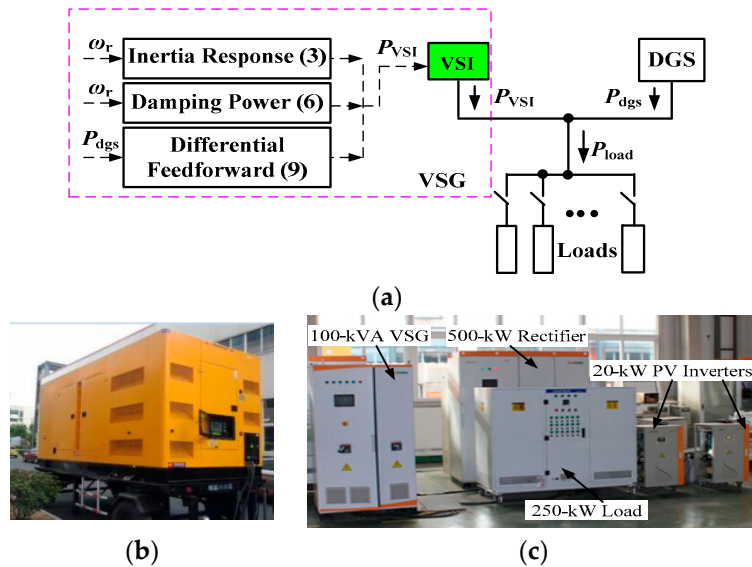


Figure 16. Experimental platform. (a) An autonomous microgrid with a DGS and a VSG unit; (b) A 400 kW DGS; (c) The VSG system.

(1) Virtual inertia: The performance of increasing virtual inertia is shown in Figure 17a, where it can be found that the system frequency oscillates for a longer time. When the dynamic frequency support is complemented by the virtual inertia control loop (with $J = 2 \text{ kg}\cdot\text{m}^2$, $J = 4 \text{ kg}\cdot\text{m}^2$, and

$J = 6 \text{ kg}\cdot\text{m}^2$), the VSG outputs dynamic active power. As a result, both the MFD and the RoCoF are decreased, as shown in Figure 17b. For $J = 6 \text{ kg}\cdot\text{m}^2$, the MFD is decreased from 0.58 Hz to 0.53 Hz, and the maximum RoCoF is decreased from 8.4 Hz/s to 6.0 Hz/s.

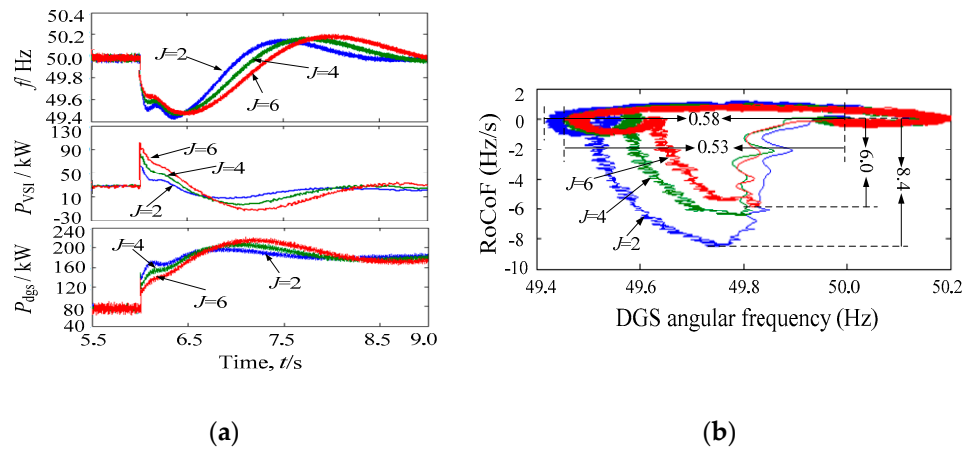


Figure 17. (a) Experimental results of the different values of virtual inertia and zero virtual damping on an active power transient; (b) Angular frequency-acceleration curves of DGS with virtual inertia control loop.

(2) Virtual damping: Figure 18a displays the experimental results for the alterations of the system frequency, the output active powers of the VSG, and the DGS. It is observed that the advantages of increasing virtual damping are the attenuation of the amplitude of the oscillations of the frequency and the reduction of the MFD.

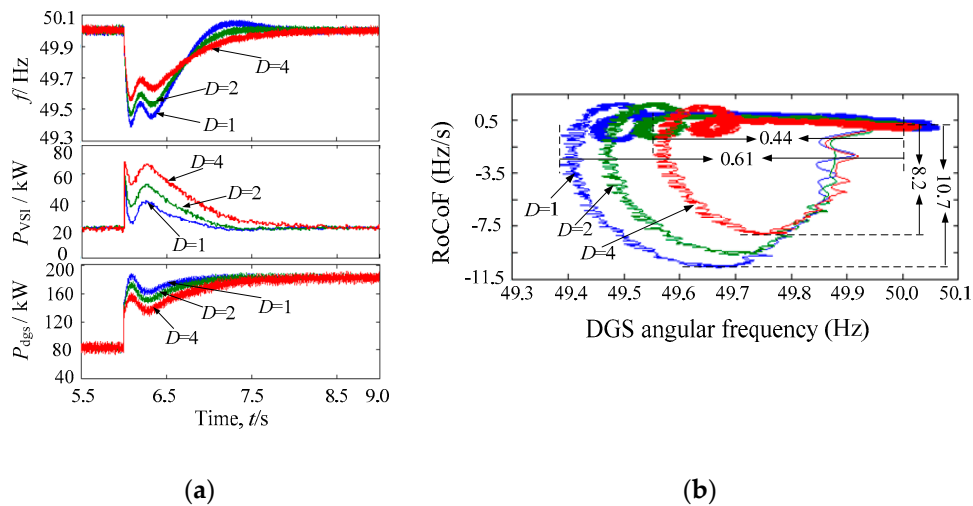


Figure 18. (a) Experimental results of the different values of virtual damping and zero virtual inertia on a power transient; (b) Angular frequency-acceleration curves of DGS with virtual damping control loop.

When the dynamic frequency support is complemented by the virtual damping control loop (with $D = 1, D = 2$, and $D = 4$), the VSG outputs dynamic active power. As a result, both the MFD and the RoCoF are decreased, as shown in Figure 18b. For $D = 4$, the MFD is decreased from 0.61 Hz to 0.44 Hz, and the maximum RoCoF is decreased from 10.7 Hz/s to 8.2 Hz/s.

(3) Differential feedforward: Figure 19a displays the experimental results for the alterations of the system frequency, the output active powers of the VSG, and the DGS. It is observed that the advantages

of adding the differential feedforward gain are the attenuation of the amplitude of the oscillations of the frequency and the reduction of the MFD.

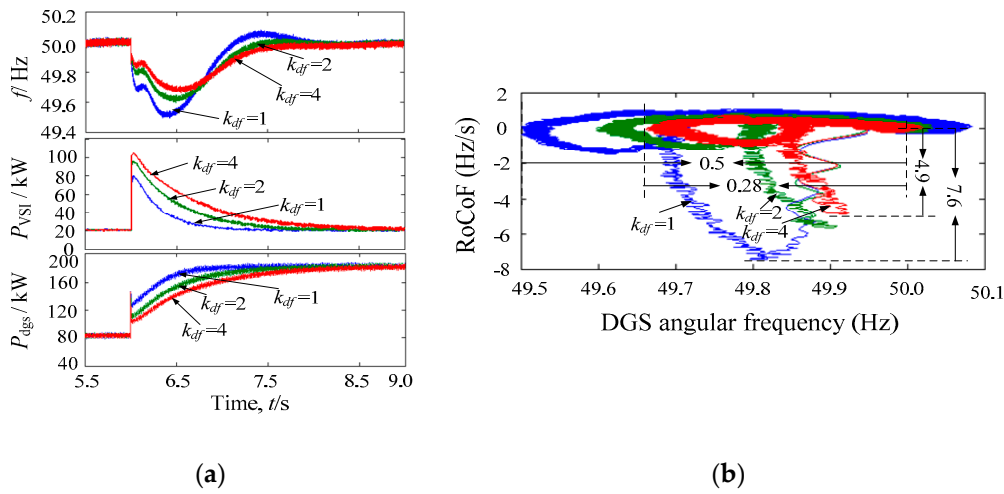


Figure 19. (a) Experimental results of the different differential feedforward gains ($D = 0$ and $J = 0$) on an active power transient; (b) Angular frequency-acceleration curves of DGS with differential feedforward control loop.

On the other hand, when the dynamic frequency support is complemented by the differential feedforward control loop (with $k_{df} = 1$, $k_{df} = 2$, and $k_{df} = 4$), the VSG outputs dynamic active power. As a result, both the MFD and the RoCoF are decreased, as shown in Figure 19b. For $k_{df} = 4$, the MFD is reduced from 0.5 Hz to 0.28 Hz, and the maximum RoCoF is reduced from 7.6 Hz/s to 4.9 Hz/s.

C. Summary

Table 3 summarizes the experimental results. Absolute error is calculated only between the maximum value and the minimum value as $(x_{\max} - x_{\min})$. To compare the performances of the virtual inertia, the virtual damping, and the differential feedforward, two indexes that give a survey of how much energy is applied from the ESS to decrease the MFD and the RoCoF are defined as

$$\begin{cases} I_{perf} = \frac{E_{AE}}{MFD_{AE}} = \frac{E_{de} - E_{re}}{MFD_{\max} - MFD_{\min}} \text{ [kJ/Hz]} \\ I_{perdf} = \frac{E_{AE}}{RoCoF_{AE}} = \frac{E_{de} - E_{re}}{RoCoF_{\max} - RoCoF_{\min}} \text{ [kJ/(Hz/s)]} \end{cases} \quad (12)$$

where E_{AE} is the absolute error between the delivered energy E_{de} and the recovered energy E_{re} of the VSG, MFD_{AE} is the absolute error of the MFD, and $RoCoF_{AE}$ is the absolute error of the RoCoF.

Table 3. Performance comparison among virtual inertia, virtual damping, and differential feedforward under load step.

Control Type	MFD_{AE} (Hz)	$RoCoF_{AE}$ (Hz/s)	E_{AE} (kJ)
Virtual inertia	0.05	2.4	11.3
Virtual damping	0.17	2.5	29.6
Differential feedforward	0.22	2.7	26.8

Table 4 displays the calculated results of I_{perf} and I_{perdf} for the VSG for the different experimental scenarios. It can be found that the virtual inertia control is more efficient in reducing the RoCoF than the other control methods, but it uses more energy in reducing the MFD. On the other hand, it can be found that the values calculated for the VSG with the differential feedforward control are continuously

smaller than the values calculated for the VSG with the virtual damping control. This illustrates that the differential feedforward control uses less energy in reducing the MFD than the virtual damping control, using approximately 70% of the delivered energy. In addition, the differential feedforward control uses less energy in reducing the RoCoF than the virtual damping control, using approximately 84% of the delivered energy, i.e., is more effective in supporting dynamic frequency control.

Table 4. Performance indexes for virtual inertia, virtual damping, and differential feedforward under load step.

Control Type	I_{perf} (kJ/Hz)	I_{perdf} (kJ/(Hz/s))
Virtual inertia	226	4.71
Virtual damping	174.1	11.84
Differential feedforward	121.8	9.93

On the other hand, with the differential feedforward control, the system presented is more effective in reducing the MFD than the virtual inertia control, using approximately 54% of the delivered energy, however, it uses only 45% of energy in reducing the RoCoF used by the virtual inertia control.

6. Conclusions

The dynamic frequency support control for the autonomous PV–diesel hybrid microgrids with the ESS based on VSG is investigated in this paper. The performances of the virtual inertia, the virtual damping, as well as the differential feedforward are evaluated by comparing their reductions in the MFD and the RoCoF for the simulation and experimental scenarios. For experimental cases, the virtual inertia control is more efficient in reducing the RoCoF than the other control methods, but uses more energy in reducing the MFD. Meanwhile, a side effect of increasing virtual inertia is that the system becomes more oscillatory and slower. On the other hand, the differential feedforward control achieves the same performance to that of the virtual damping control while reducing the MFD and the RoCoF. Moreover, in all the experimental scenarios, the differential feedforward control uses less energy in reducing the MFD and the RoCoF than the virtual damping control, i.e., is more effective in supporting dynamic frequency control.

Finally, it was also found that, depending on the type of load variation, the operation of the proposed differential feedforward control may lead to a greater charge/discharge of the ESS when compared to the virtual inertia control. This suggests that further work is required in order to include the state of health and the state of charge of the ESS for the differential feedforward control. Also, a stability analysis is required in order to know the admissible values for k_{df} .

Author Contributions: R.S. designed the algorithm and performed the experiments and conducted simulations as the first author. X.Z. handled the project and contributed materials tools. All the authors approved the publication.

Funding: This research received no external funding.

Acknowledgments: This work was supported by the National key Research and Development Program of China (No. 2016YFB0900300), and the National Natural Science Foundation of China (No. 51677049).

Conflicts of Interest: The authors declare no conflict of interest.

Nomenclatures

P_{VSIi}	active power of the VSI unit ($i = 1-2$)
P_{dgs}	active power of the DGS
P_{PV}	active power of the PV generator
P_{load}	active power of the load
J_{dg}	rotating inertia of the DGS
ω_r	rotor angular speed
k_{loss}	rotational losses

ω_{r0}	synchronous speed
P_M	mechanical power
k_{pm}	gain of fuel injection system and diesel engine
τ_{pm}	time constant of the fuel injection system
τ_d	dead time of the diesel engine
k_{dp}	proportional factors of a PI controller
k_{di}	integral factors of a PI controller
J	virtual inertia
J_{eq}	total inertia
ω_{ni}	natural oscillation frequency ($i = 1-3$)
ζ_i	damping ratio ($i = 1-3$)
D	virtual damping
k_{df}	differential feedforward gain
τ	filtering time gain of the low-pass filter (LPF)
λ_i	conjugate eigenvalues ($i = 1-3$)
E_{AE}	absolute error
E_{de}	delivered energy
E_{re}	recovered energy
MFD_{AE}	absolute error of the MFD
$RoCoF_{AE}$	absolute error of the RoCoF
I_{perf}	energy index of the MFD
I_{perdf}	energy index of the RoCoF

References

1. Torres, M.; Lopes, L.A.C. Virtual synchronous generator control in autonomous wind-diesel power systems. In Proceedings of the IEEE Electrical Power & Energy Conference (EPEC), Montreal, QC, Canada, 22–23 October 2009.
2. Nacfaire, H. *Wind-Diesel and Wind Autonomous Energy Systems*; Elsevier Science: New York, NY, USA, 1989.
3. Committee E M. *IEEE Recommended Practice for Monitoring Electric Power Quality (Revision of IEEE Std 1159–1995)*; IEEE: New York, NY, USA, 2009.
4. Torres, L.M.A.; Lopes, L.A.; Moran, T.L.A.; Espinoza, C.J.R. Self-tuning virtual synchronous machine: A control strategy for energy storage systems to support dynamic frequency control. *IEEE Trans. Energy Convers.* **2014**, *29*, 833–840. [[CrossRef](#)]
5. Li, W.; Joos, G.; Abbey, C. Wind power impact on system frequency deviation and an ESS based power filtering algorithm solution. In Proceedings of the IEEE PES Power Systems Conference and Exposition, Atlanta, GA, USA, 29 October–1 November 2006.
6. Tao, Y.; Liu, Q.; Deng, Y.; Liu, X.; He, X. Analysis and mitigation of inverter output impedance impacts for distributed energy resource interface. *IEEE Trans. Power Electron.* **2015**, *30*, 3563–3576. [[CrossRef](#)]
7. Vasquez, J.C.; Guerrero, J.M.; Savaghebi, M.; Eloy-Garcia, J.; Teodorescu, R. Modeling, analysis, and design of stationary-reference-frame droop-controlled parallel three-phase voltage source inverters. *IEEE Trans. Ind. Electron.* **2013**, *60*, 1271–1280. [[CrossRef](#)]
8. Han, Y.; Shen, P.; Zhao, X.; Guerrero, J.M. An enhanced power sharing scheme for voltage unbalance and harmonics compensation in an islanded AC microgrid. *IEEE Trans. Energy Convers.* **2016**, *31*, 1037–1050. [[CrossRef](#)]
9. Guerrero, J.M.; Vasquez, J.C.; Matas, J.; Castilla, M.; Vicuña, L.G.D.; Castilla, M. Hierarchical control of droop-controlled AC and DC microgrids-A general approach toward standardization. *IEEE Trans. Ind. Electron.* **2011**, *58*, 158–172. [[CrossRef](#)]
10. Matas, J.; Castilla, M.; de Vicuna, L.G.; Miret, J.; Vasquez, J.C. Virtual impedance loop for droop-controlled single-phase parallel inverters using a second-order general-integrator scheme. *IEEE Trans. Power Electron.* **2010**, *25*, 2993–3002. [[CrossRef](#)]
11. Liu, J.; Miura, Y.; Ise, T. Comparison of dynamic characteristics between virtual synchronous generator and droop control in inverter-based distributed generators. *IEEE Trans. Power Electron.* **2016**, *31*, 3600–3611. [[CrossRef](#)]

12. Shintai, T.; Miura, Y.; Ise, T. Oscillation damping of a distributed generator using a virtual synchronous generator. *IEEE Trans. Power Deliv.* **2014**, *29*, 668–676. [[CrossRef](#)]
13. Zhong, Q.-C.; Weiss, G. Synchronverters: Inverters that mimic synchronous generators. *IEEE Trans. Ind. Electron.* **2011**, *58*, 1259–1267. [[CrossRef](#)]
14. Bevrani, H.; Ise, T.; Miura, Y. Virtual synchronous generators: A survey and new perspectives. *Int. J. Electr. Power Energy Syst.* **2014**, *54*, 244–254. [[CrossRef](#)]
15. Guan, M.; Pan, W.; Zhang, J.; Hao, Q.; Cheng, J.; Zheng, X. Synchronous generator emulation control strategy for voltage source converter (VSC) stations. *IEEE Trans. Power Syst.* **2015**, *30*, 3093–3101. [[CrossRef](#)]
16. Yuko, H.; Kazushige, S.; Kenichi, S.; Toshifumi, I. Analysis of resonance in microgrids and effects of system frequency stabilization using a virtual synchronous generator. *IEEE J. Emerg. Sel. Top. Power Electron.* **2016**, *4*, 1287–1298.
17. Shi, R.L.; Zhang, X.; Liu, F.; Xu, H.; Hu, C.; Ni, H.; Yu, Y. A differential feedforward control of output current for high performance virtual synchronous generator. In Proceedings of the IEEE 2nd International Future Energy Electronics Conference (IFEEEC), Taipei, Taiwan, 1–4 November 2015.
18. Liu, J.; Miura, Y.; Bevrani, H.; Ise, T. Enhanced virtual synchronous generator control for parallel inverters in microgrids. *IEEE Trans. Smart Grid* **2016**, *8*, 2268–2277. [[CrossRef](#)]
19. Hirase, Y.; Noro, O.; Sugimoto, K.; Sakimoto, K.; Shindo, Y.; Osaka, T.I. Effects and analysis of suppressing frequency fluctuations in microgrids using virtual synchronous generator control. In Proceedings of the 41st Annual Conference of the IEEE Industrial Electronics Society, Yokohama, Japan, 9–12 November 2015.
20. Shi, R.L.; Zhang, X.; Liu, F.; Xu, H.; Hu, C.; Yu, Y.; Ni, H. Research on power compensation strategy for diesel generator system based on virtual synchronous generator. In Proceedings of the IEEE 8th International Power Electronics and Motion Control Conference (IPEMC-ECCE Asia), Hefei, China, 22–26 May 2016.
21. Morren, J.; de Haan, S.; Kling, W.; Ferreira, J. Wind turbines emulating inertia and supporting primary frequency control. *IEEE Trans. Power Syst.* **2006**, *21*, 433–434. [[CrossRef](#)]
22. Xue, Y.; Tai, N. Review of contribution to frequency control through variable speed wind turbine. *Renew. Energy* **2011**, *36*, 1671–1677.
23. Alipoor, J.; Miura, Y.; Ise, T. Power system stabilization using virtual synchronous generator with alternating moment of inertia. *IEEE J. Emerg. Sel. Top. Power Electron.* **2015**, *3*, 451–458. [[CrossRef](#)]
24. Alipoor, J.; Miura, Y.; Ise, T. Distributed generation grid integration using virtual synchronous generator with adoptive virtual inertia. In Proceedings of the IEEE Energy Conversion Congress and Exposition, Denver, CO, USA, 15–19 September 2013.
25. Krishnamurthy, S.; Jahns, T.; Lasseter, R. The operation of diesel gensets in a certs microgrid. In Proceedings of the IEEE Power and Energy Society General Meeting—Conversion and Delivery of Electrical Energy in the 21st Century, Pittsburgh, PA, USA, 20–24 July 2008.
26. Shi, R.L.; Zhang, X.; Chao, H.; Xu, H.; Gu, J.; Cao, W. Self-tuning virtual synchronous generator control for improving frequency stability in autonomous photovoltaic-diesel microgrids. *J. Mod. Power Syst. Clean Energy* **2018**, *6*, 482–494. [[CrossRef](#)]

